Vera C. Rubin Observatory
Systems Engineering

# Impact of Including Wavelength-dependent PSF Modeling in Rubin Commissioning Data

**Aashay Pai, Pierre-François Léget, Shrihan Agarwal, and Chihway Chang**

**SITCOMTN-174**

https://doi.org/10.71929/rubin/3398709

**Latest Revision: 2026-08-03**

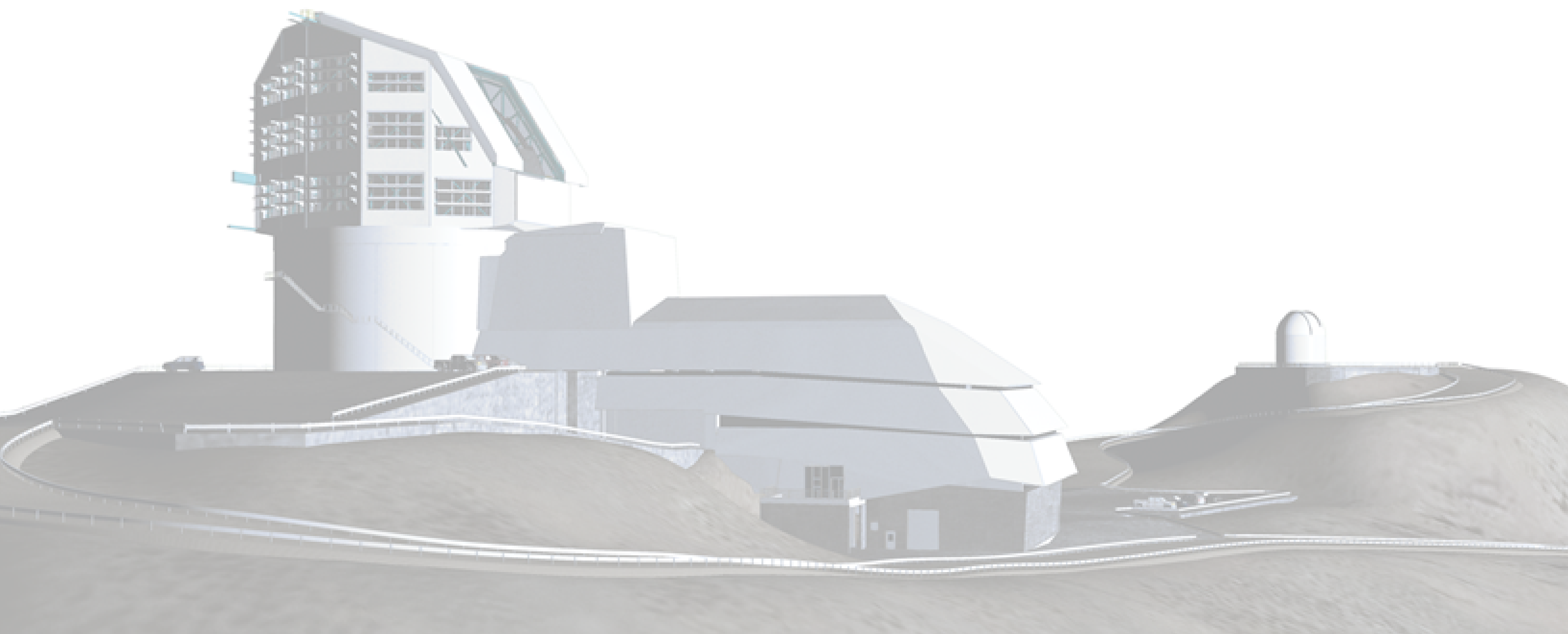

## Abstract

We present the results from enabling chromatic modelling of the Point Spread Function (PSF) during the commissioning of the Vera C. Rubin Observatory.

# Change Record

| Version | Date | Description | Owner name |
|---|---|---|---|
| 1 | 2026-03-04 | Added sections 1-6 and section 8 | Aashay Pai |
| 1 | 2026-03-04 | Added section 7 | Shrihan Agarwal |
| 2 | 2026-04-05 | Second round of edits | Aashay Pai |
| 2 | 2026-04-05 | Second round of edits | Shrihan Agarwal |
| 3 | 2026-04-26 | Removed from draft status | Aashay Pai |

*Document source location:* `https://github.com/lsst-so/sitcomtn-174`

# Contents

# Impact of Including Wavelength-dependent PSF Modeling in Rubin Commissioning Data

## 1 Introduction

Weak gravitational lensing of the large-scale structure (cosmic shear) is one of the key tools in cosmology for understanding the distribution of cosmic structures and deducting the cosmological model that gave rise to it. According to General Relativity, light is bent when it passes through gravitational perturbations sourced by cosmic structure. This means that the light rays from distant galaxies are "lensed" as they travel to us, resulting in small distortions in the observed galaxy shapes. This distortion encodes information of the cosmic structure, allowing us to probe (visible and invisible) cosmic structure.

The central observable in weak lensing is thus the shapes of galaxy images. In particular, we are interested in the galaxy shapes after it has been distorted (or lensed) by the cosmic structure but before it is distorted further by atmospheric or instrumental effects. As this exact quantity is not observable, we can only derive it by having a good model of the atmospheric and instrumental effects, or the Point Spread Function (PSF).

The PSF refers to how a point source will look like on our detectors at a given time and location on the focal plane. It encodes the net effect from the atmosphere, the optics and the detectors and can be thought of as a convolution kernel (or a Green's function) that is applied to the light that comes into the telescope. Having a precise and accurate PSF model for each galaxy is key to the success of weak lensing science for Rubin LSST.

One of the subtleties in modeling the PSF is that the PSF is wavelength-dependent. In particular, Differential Chromatic Refraction (DCR, Sullivan & Reiss, DMTN-017; Plazas & Bernstein, 2012; Meyers & Burchat, 2015) and chromatic seeing are the dominating wavelength-dependent PSF effects that exist in ground-based imaging instruments such as Rubin's LSSTCam. When we look through the atmosphere at different airmass, the light rays that enter the atmosphere come in a non-perpendicular incident angle and refraction happens at the interface. Blue light refracts more than red light, causing small distortions or displacements of the observed objects that depend on their wavelength. This tech note focuses on this effect and how we could model it in the Rubin pipeline.

The Rubin Observatory uses a PSF fitting strategy adapted from the Dark Energy Survey (DES), which is based on the PSF in the Full Focal plane (PiFF) algorithm (Jarvis et al., 2021). In this note we examine the performance of the PSF modeling in the Rubin commissioning data. We use the weekly intermittent LSST Science Pipelines (Rubin Observatory Science Pipelines Developers, PSTN-019) `w_2025_49` data.

The structure of this note is as follows. Section 2 describes the DCR effect. Section 3 describes the data products used in this study. Section 4 discusses the fitting procedure, PSF residual definitions and the PSF fitting configuration. Section 5 shows the results of enabling chromatic fitting on PSF residuals. In Section 6 we compare our results with that from DES and in Section 7 propagate the PSF residuals to expected residuals in shear measurements (we only consider additive biases due to DCR and not multiplicative biases due to chromatic seeing).

## 2 Differential Chromatic Refraction

As light passes through the Earth's atmosphere, it is refracted toward the zenith. The magnitude of this refraction is wavelength-dependent, with shorter (bluer) wavelengths experiencing stronger refraction than longer (redder) wavelengths. This chromatic dependence leads to small, band-dependent shifts in the measured positions of astronomical objects, which in turn propagate into the modeling of the point-spread function (PSF). Equation 1 defines $DCR_1$ and $DCR_2$ as the components of the differential chromatic refraction along the $e_1$ and $e_2$ directions, respectively, expressed as functions of the zenith angle $z$ and the parallactic angle $q$. To compute the DCR, we first determine the local sidereal time for each visit and use it to calculate $z$ and $q$ for every star.

$$\begin{aligned} \mathrm{DCR}_1 &\equiv \tan^2(z)\cos(2q) \\ \mathrm{DCR}_2 &\equiv \tan^2(z)\sin(2q) \end{aligned} \tag{1}$$

## 3 Data

In this study, we use data products generated by the weekly intermittent Data Release Production (DRPs). These DRPs aim to test current data quality and produce LSST-like downstream data from the single-visit exposures. The week 49 DRP processed 4898 visits collected between 2025-04-17 and 2025-09-21 over an area of $\sim 130\,\mathrm{deg}^2$. We only use visits labelled as ”science” visits. Figure 1 shows the footprint of the data processed in the week 49 DRP This DRP processed visits from the COSMOS, M49, SV225_40, ELAIS_S1, ECDFS and EDFS A + B fields. It does not include the LSST SV1000 region.

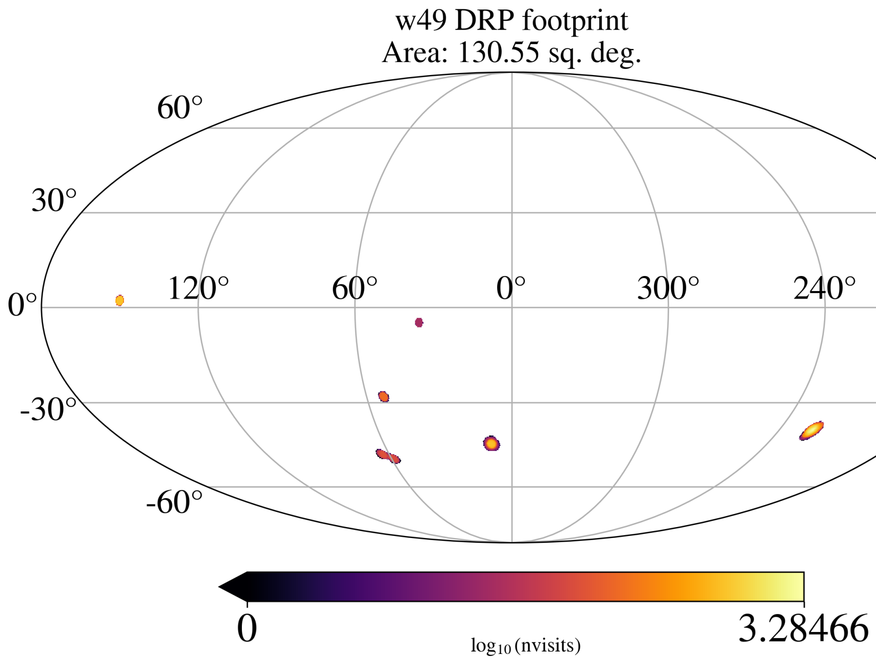


Figure 1: week 49 DRP footprint, coloured by the number of visits collected in the pixel.

We use two main data products: the `object` and the `refit_psf_star` tables.

The `object` table contains data of stars and galaxies derived from the per-band coadded images. The `refit_psf_star` table contains data of stars and galaxies derived from the single-visit images and PSF moments modelled with the `PiFF` package (Jarvis et al., 2021). For the purposes of this technote, we transform the moments from camera coordinates (as defined in the catalogs) into celestial coordinates (RA/Dec).

For measured second-order moments, we use `slot_Shape_xx`, `slot_Shape_yy` and `slot_Shape_xy` that have been measured using the HSM method (Hirata & Seljak, 2003; Mandelbaum et al., 2005, 2018) in which the moments are determined using an iterative elliptical Gaussian fit. For the second-order moments of the `PiFF` PSF model, we use `slot_PsfShape_xx`, `slot_PsfShape_yy` and `slot_PsfShape_xy`, also derived using the HSM shape algorithm.

For star magnitudes, we use calibrated magnitudes (`ap12Flux_mag`) from the `refit_psf_star` table. For magnitudes that are used to calculate colour, we use band-calibrated magnitudes from the `object` tables.

## 4 PSF Characterization

In this section we give a brief overview of the PSF fitting procedure used by `PiFF`, our definitions of PSF related quantities and the fitting configuration used for the data.

### 4.1 Fitting

For a given single-visit image processed by the DRP, the PSF is fit independently on each CCD. Under the default DRP configuration, which does not include chromatic corrections, the PSF modeling is performed using `PiFF`. The input to `PiFF` is a catalog of all detected objects in the image, together with their positions in sky coordinates. From this catalog, `PiFF` selects two subsets of stars: a primary sample used to fit the PSF model and a smaller, reserved sample used for PSF diagnostic tests. A model is then fit to the stellar images to obtain a maximum-likelihood estimate of the PSF parameters (position, and optionally, wavelength) at each stellar location. Finally, the fitted model parameters are interpolated across the stellar sample to estimate the PSF over the full focal plane using a second order polynomial. To incorporate colour dependence in the PSF modeling, we provide `PiFF` with stellar colours derived using the Forward Global Calibration Method (FGCM; Burke et al., 2018), which are computed in a preceding step of the DRP.

### 4.2 PSF Shape Definitions

Equation 2 shows the definitions for PSF size ($T$) and ellipticity ($e_1$ & $e_2$) that are used in this work.

$$\begin{aligned} T &\equiv i_{xx} + i_{yy} \\ e_1 &\equiv \frac{i_{xx} - i_{yy}}{i_{xx} + i_{yy}} \\ e_2 &\equiv \frac{2i_{xy}}{i_{xx} + i_{yy}} \end{aligned} \tag{2}$$

For each quantity above ($T$, $e_1$, $e_2$), we also define the residual to be the difference between the measured value and the fit value of the model: $\delta X \equiv X_{\mathrm{PSF}} - X_{\mathrm{model}}$ and $\delta X/X \equiv (X_{\mathrm{PSF}} - X_{\mathrm{model}})/X_{\mathrm{PSF}}$.

### 4.3 PSF Fitting Configuration

We test several PiFF chromatic fitting configurations to minimize the error in the PSF model due to chromatic effects. We saw most improvement in the PSF fit by using a 2nd-order polynomial fit in spatial position and colour, with no significant improvement from using higher orders. The final configuration is shown below.

```
config.psf_determiner['piff'].spatialOrderPerBand = {
  "u": 2, "g": 2, "r": 2, "i": 2, "z": 2, "y": 2,
}
config.psf_determiner['piff'].zerothOrderInterpNotEnoughStars = False
config.psf_determiner['piff'].piffBasisPolynomialSolver = "cpp"
config.psf_determiner['piff'].piffPixelGridFitCenter = False
config.psf_determiner['piff'].useColor = True
config.psf_determiner['piff'].colorOrder = 2
config.psf_determiner['piff'].color = {
  "u": "g-i", "g": "g-i", "r": "g-i", "i": "g-i",
  "z": "i-z", "y": "i-z",
}
```

## 5 Results

In this section, we study PSF size and ellipticity residuals as a function of magnitude, sky position (DCR), and colour. We use data from the week 49 DRP[1], which contains 4898 visits and $\sim$ 153 million source detections. We perform the measurements using all stars, and we use stars binned by $g - i$ colour in 3 equally distributed bins to quantify the colour-dependent effects. We show how the PSF model improves when enabling chromatic fitting of the PSF in PiFF. This analysis was performed on the Rubin Science Platform (RSP) at the US Data Facility (USDF).

[1] collection: LSSTCam/runs/DRP/20250417_20250921/w_2025_49/DM-53545

## 5.1 Residuals by magnitude

Figure 2 shows the PSF $\delta T/T$, $\delta e_1$ and $\delta e_2$ residuals as a function of star magnitude. The stars have been divided into colour bins of $g - i \in [0.66, 0.94, 1.78, 3.5]$.

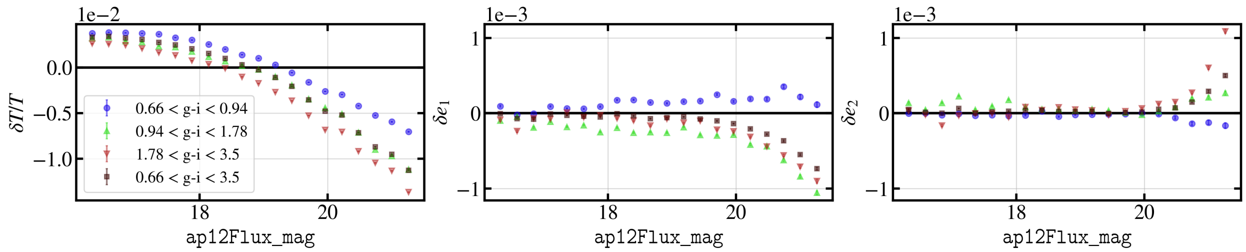


(a) without chromatic PSF fitting.

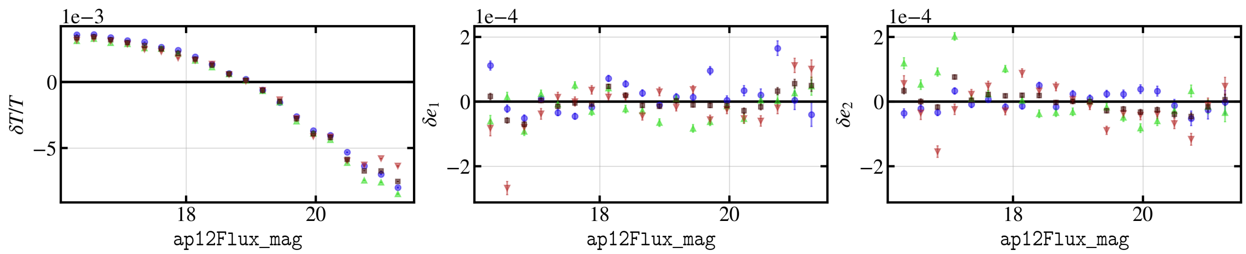


(b) with chromatic PSF fitting.

Figure 2: PSF $\delta T/T$, $\delta e_1$ and $\delta e_2$ as a function of ap12Flux_mag before (a) and after (b) turning on chromatic PSF fitting. Note that the y-axis ranges in (a) and (b) are different. Stars are divided into equal-sized colour bins of $g - i \in [0.66, 0.94, 1.78, 3.5]$. Enabling chromatic PSF reduces the spread or residuals between colour bins.

Without chromatic fitting, the spread in $\delta e_1$ at the faint end is $\sim 3\times$ larger than that of $\delta e_2$. Enabling chromatic fitting of the PSF tightens and thereby reduces the spread in the residuals toward the faint end in all colour bins, but is most prominently seen in $\delta e_1$. As expected, the magnitude of the errors are not reduced by chromatic fitting, but the spread between the individual colour bins is reduced, which can be most clearly seen in $\delta T/T$.

Figure 3 shows the residuals of PSF $\delta T/T$, $\delta e_1$ and $\delta e_2$ as a function of star magnitude for visits in the $g$ band only, where we expect to see the most significant chromatic PSF effect. The stars are divided into colour bins of $g - i \in [0.65, 0.87, 1.39, 3.5]$. Enabling chromatic fitting reduces $\delta T/T$ residuals by $\sim$ 50%. For $\delta e_1$ and $\delta e_2$, chromatic fitting tightens the residuals at the faint end (mag > 18) by $\sim$ 75%. It is comparatively ineffective in tightening the reddest colour bin at the bright end.

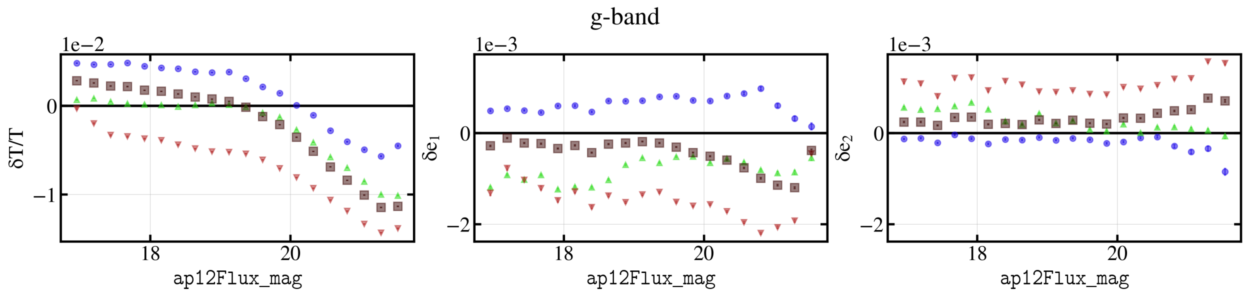


(a) without chromatic PSF fitting.

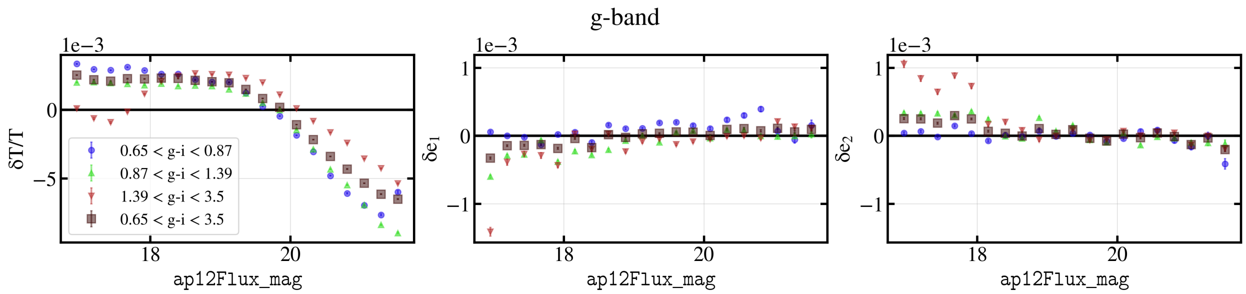


(b) with chromatic PSF fitting.

Figure 3: PSF $\delta T/T$, $\delta e_1$ and $\delta e_2$ for $g$ band visits only as a function of `ap12Flux_mag` before (a) and after (b) turning on chromatic PSF fitting. Note that the y-axis ranges in (a) and (b) are different. Stars are divided into equal-sized colour bins of $g - i \in [0.65, 0.87, 1.39, 3.5]$. Enabling chromatic PSF shows the most improvement in the residuals in the blue, faint objects.

## 5.2 Residuals by colour

Figure 4 plots the PSF $\delta T/T$, $\delta e_1$ and $\delta e_2$ residuals as a function of $g - i$ colour. Subfig. 4c shows the number density of stars as a function of $g - i$ colour, which is common to both subfigures 4a. and 4b. The residuals of $\delta T/T$ and $\delta e_1$ show the strongest colour dependence in the $u$ and $g$ bands respectively. Chromatic fitting corrects the colour dependence in the $g$ band, but is ineffective in correcting the $u$ band colour dependence. However, this could be due to the lack of enough objects in the $u$ band in red $g - i$ bins, as can be seen in the histogram. The discrepancy between the trends of $\delta e_1$ and $\delta e_2$ residuals could also be due to the non-isotropic distribution of parallactic angles leading to different mean values of $\cos 2q$ and $\sin 2q$, which are the relevant scaling quantities for $\delta e_1$ and $\delta e_2$ respectively. For the data in the week 49 DRP, $\langle \cos 2q \rangle = -0.29$ and $\langle \sin 2q \rangle = -0.17$. These plots of the parallactic angle are shown in Appendix E.

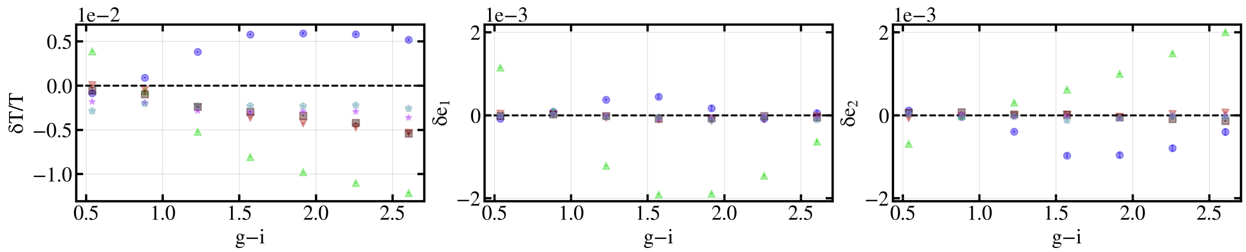


(a) without chromatic PSF fitting.

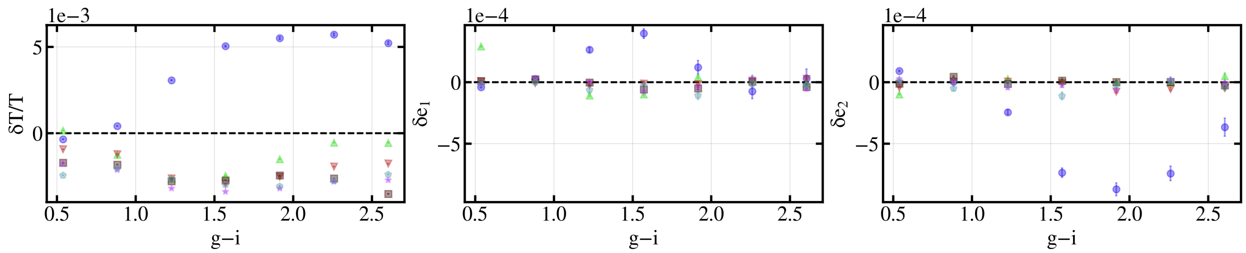


(b) with chromatic PSF fitting.

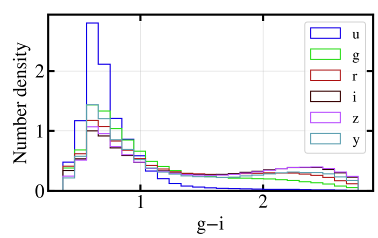


(c) Number density as a function of $g-i$ colour.

Figure 4: PSF $\delta T/T$, $\delta e_1$ and $\delta e_2$ as a function of $g-i$ colour. The $u$ and $g$ band residuals show the highest dependence on $g-i$ colour. Note that the y-axis ranges in (a) and (b) are different. Enabling chromatic fitting corrects the $g$ band colour dependence, but is unable to correct the $u$ band dependence, possibly due to the small number of observations with red $g-i$ colour.

## 5.3 Residuals by Position (DCR)

Figure 5 shows the PSF $\delta e_1$ and $\delta e_2$ as a function of DCR$_1$ and DCR$_2$ respectively for observations in the $g$ band, which is affected the most by DCR. The stars are separated in colour bins of $g-i \in [0.64, 0.85, 1.5, 3.5]$. Chromatic fitting of the PSF corrects DCR dependent residuals by up to $\sim$ 90% in $\delta e_1$ and up to $\sim$ 95% in $\delta e_2$, therefore reducing DCR dependent errors by almost an order of magnitude.

Figure 6 shows the PSF $\delta e_1$ and $\delta e_2$ as a function of DCR$_1$ and DCR$_2$ respectively for observations in the $r$ band. The stars are separated in colour bins of $g-i \in [0.64, 0.85, 1.5, 3.5]$. Chromatic fitting of the PSF corrects DCR dependent residuals by up to $\sim$ 50% in $\delta e_1$ and $\delta e_2$.

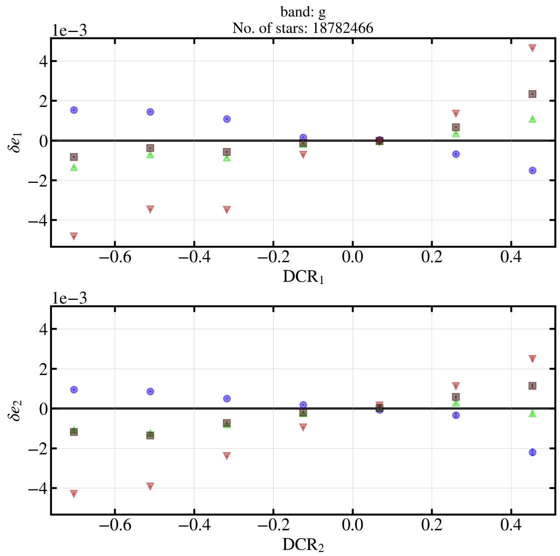


(a) without chromatic PSF fitting.

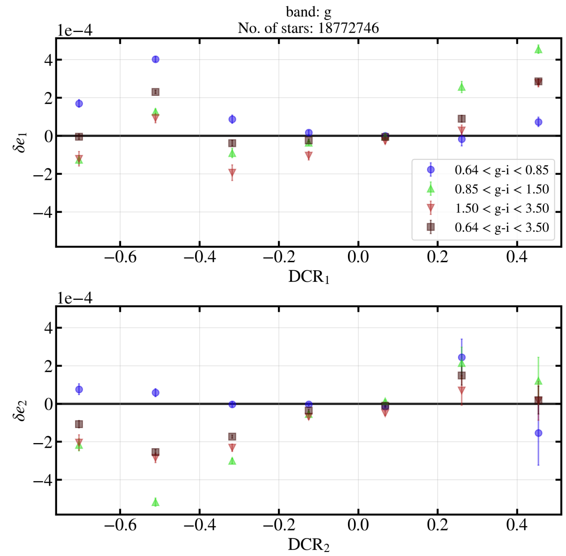


(b) with chromatic PSF fitting.

Figure 5: PSF $\delta e_1$ and $\delta e_2$ as a function of $\mathrm{DCR}_1$ and $\mathrm{DCR}_2$ respectively before (a) and after (b) turning on chromatic PSF fitting. Note that the y-axis ranges in (a) and (b) are different. Chromatic fitting of the PSF reduces residuals by up to $\sim 95\%$ in the *g* band.

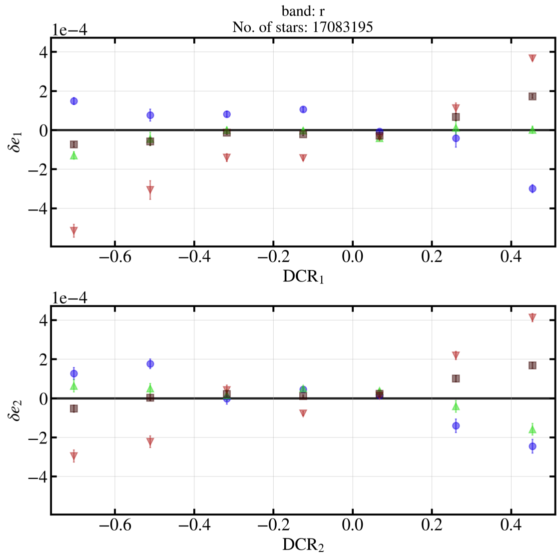


(a) without chromatic PSF fitting.

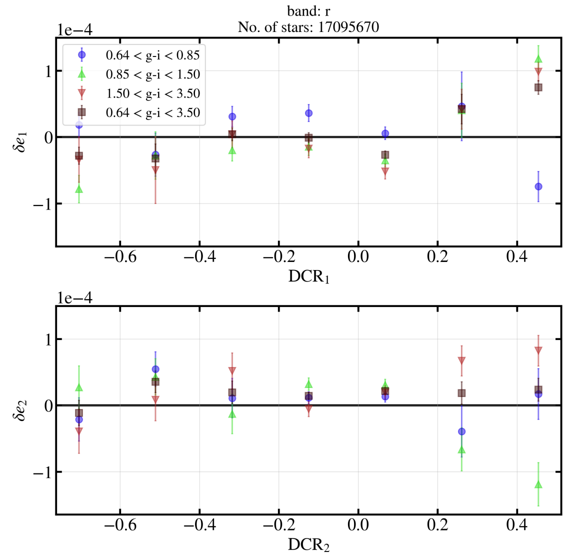


(b) with chromatic PSF fitting.

Figure 6: PSF $\delta e_1$ and $\delta e_2$ as a function of $\mathrm{DCR}_1$ and $\mathrm{DCR}_2$ respectively before (a) and after (b) turning on chromatic PSF fitting. Note that the y-axis ranges in (a) and (b) are different. Chromatic fitting of the PSF reduces residuals by up to $\sim$50% in the *r* band.

We also transform PSF moments from celestial coordinates into the altitude/azimuth frame of the telescope. Equation 3 defines residuals in this frame that are similar to $\delta e_1$ and $\delta e_2$ in celestial coordinates, but without the trace normalizing factors in Eq. 2.

$$\begin{aligned} \delta e_1 &\sim \delta I_{xx} - \delta I_{yy} \\ \delta e_2 &\sim 2\delta I_{xy} \end{aligned} \tag{3}$$

Here, the subscript 'x' stands for altitude and 'y' for azimuth. This projects the moments such that the DCR effect is captured completely along the altitude axis – where the PSF is stretched proportionally to $\tan^2 z$ (where $z$ is the zenith angle).

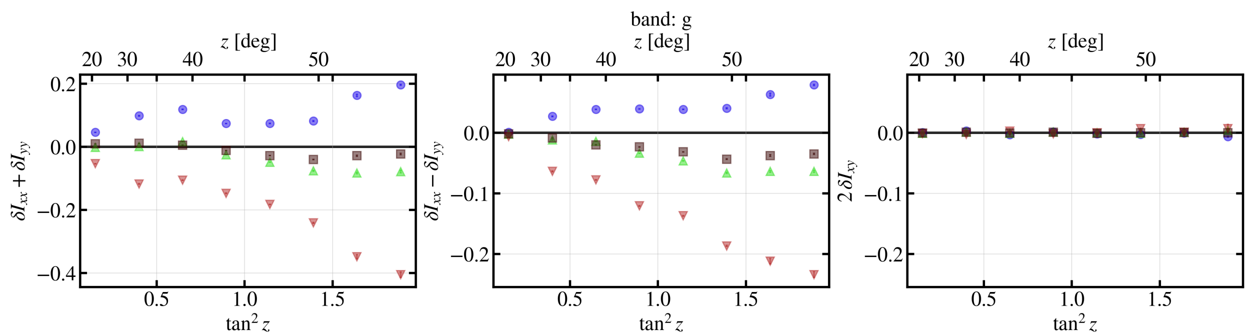


(a) without chromatic PSF fitting.

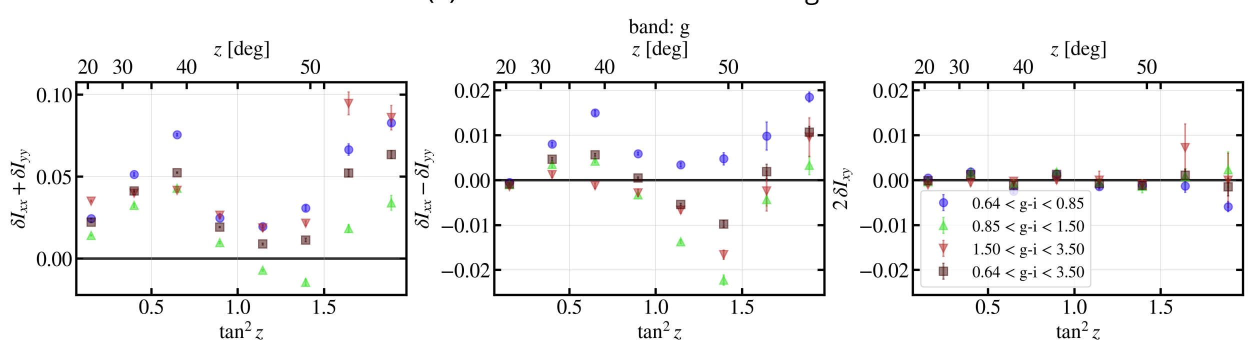


(b) with chromatic PSF fitting.

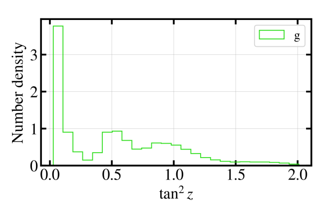


(c) Distribution of $\tan^2 z$ in $g$ band.

Figure 7: Residuals (in Alt/Az coordinates) vs. $\tan^2 z$ in $g$ band. The leftmost panel shows the trace residual $\delta T$, and the other two panels show residuals defined in Eq. 3. Chromatic fitting reduces residuals by almost an order of magnitude.

Figure 7 shows residuals vs. $\tan^2 z$ in $g$ band. The DCR effect is captured entirely along the altitude axis shown which can be seen in the middle plot. The residual along the azimuth axis (rightmost plot) is completely independent of DCR. Subfigure 7c shows the distribution of $\tan^2 z$ in the week 49 DRP data common to both Subfigs. 7a and 7b.

## 6 Comparison to the Dark Energy Survey

The Dark Energy Survey (DES) was a six-year optical and near-infrared imaging survey designed to investigate the origin of cosmic acceleration. DES operated from 2013 to 2019 using the Dark Energy Camera (DECam) mounted on the $4$ m Victor M. Blanco Telescope at Cerro Tololo Inter-American Observatory in Chile. DECam, the camera used to conduct the survey, is a 570-megapixel wide-field imager with a $\sim 3\,\mathrm{deg}^2$ field of view, consisting of 62 science CCDs. The survey imaged approximately $5000\,\mathrm{deg}^2$ of the southern sky in five broadband filters (*grizY*) to a typical depth of $i \approx 24$ mag (10$\sigma$ for galaxies).

The PSF pipelines used by the Rubin Observatory are modelled after the DES pipelines, including the use of the same PSF modelling software: `PiFF`. As the two surveys share similar science goals, we compare current Rubin Observatory PSF characteristics to DES Year 6 PSF results (Schutt et al., 2025). The DES Y6 PSF star sample consists of $\sim$ 110 million stars, while the Rubin week 49 DRP data contains $\sim$ 153 million source detections. Note that the DES Y6 colour fitting was done with a first order polynomial, while this work uses a second order polynomial.

Figure 8 shows the dependence of chromatically-fitted PSF $\delta T/T$, $\delta e_1$ and $\delta e_2$ residuals on magnitude in DES Y6 data. Comparing the residuals to Fig. 2b, we find that the magnitude of `PiFF` residuals are on par with DES levels, even though the overall trend looks different.

Figure 9 shows the DES Y6 PSF residuals as a function of $g - i$ and $i - z$ colour. Comparing the colour dependence to Fig. 4b, DES Y6 $g$ band $\delta T/T$ residuals are up to $\sim$ 50% larger than Rubin.

Figure 10 shows the DES Y6 ellipticity residuals as a function of $\mathrm{DCR}_1$ and $\mathrm{DCR}_2$ in the $g$ and $r$ bands. Comparing these to Fig. 5b and Fig. 6b, we find that in the Rubin data, the PSF model errors coming from DCR are $\sim$ 80% lower than that in DES Y6 in the $g$ band and to similar levels in the $r$ band.

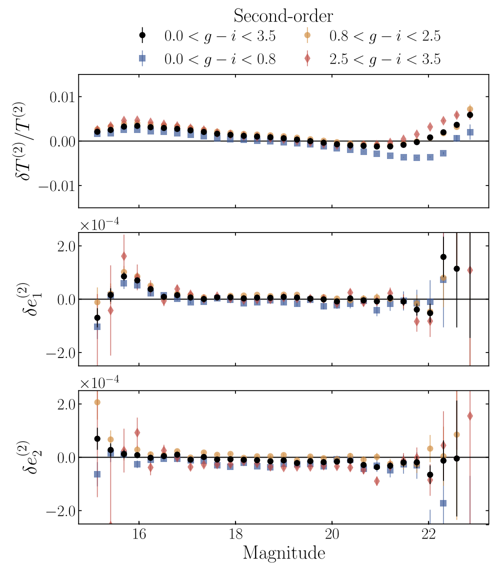


Figure 8: DES Y6 PSF $\delta T/T$, $\delta e_1$ and $\delta e_2$ as a function of magnitude. Stars are divided into equal-sized colour bins of $g-i \in [0.0, 0.8, 2.5, 3.5]$ (This plot is identical to the top three panels of Fig. 15 in Schutt et al. (2025)).

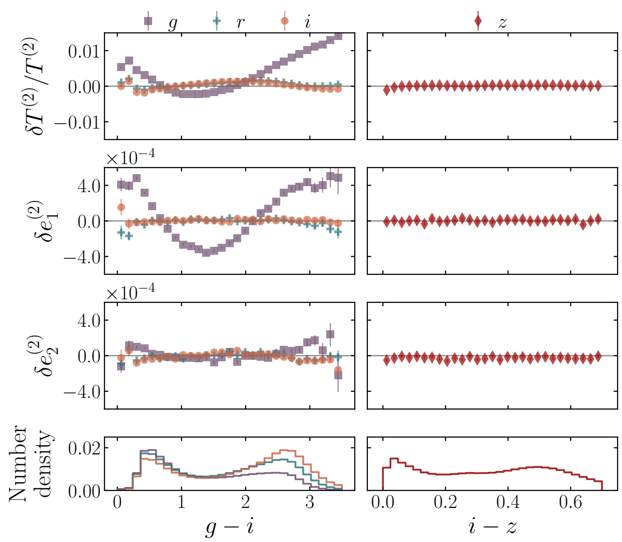


Figure 9: DES Y6 residuals as a function of $g-i$ colour (for the *gri* bands) and $i-z$ colour (for the *z* band) (This plot is identical to the four left panels of Fig. 18 in Schutt et al. (2025)).

## 7 Impact on Shear Systematics

Systematics due to DCR affect the shapes of both stars and galaxies by biasing their PSF. The amount of bias is determined by the SED of the star or galaxy within the observing band.

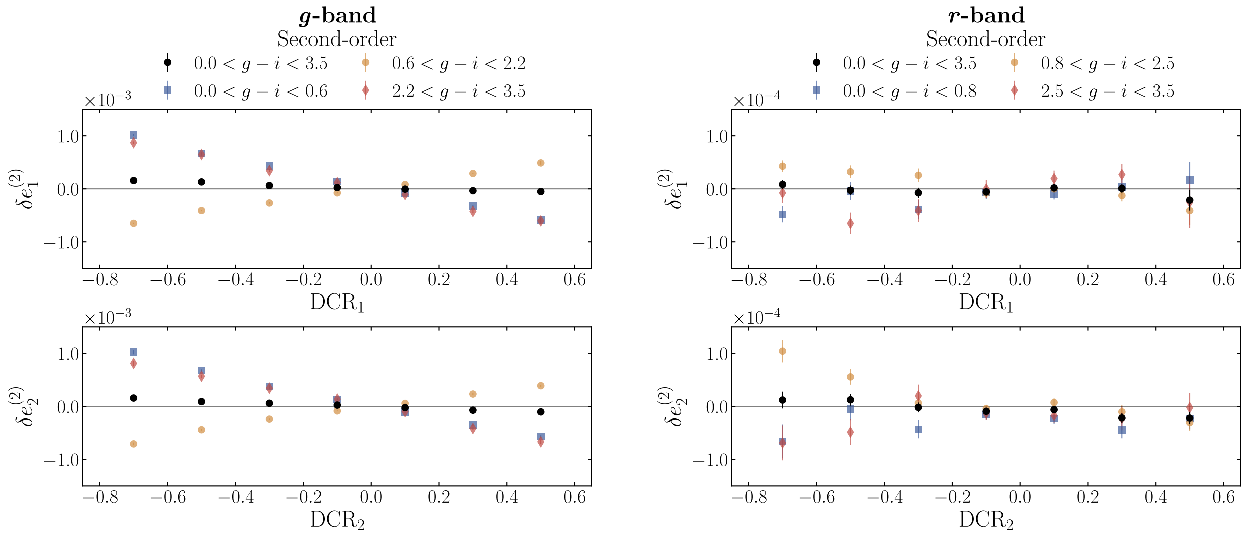


Figure 10: DES Y6 PSF $\delta e_1$ and $\delta e_2$ as a function of $\mathrm{DCR}_1$ and $\mathrm{DCR}_2$ respectively, in the $g$ and $r$ bands (This plot is identical to the top two panels of Fig. 16 in Schutt et al. (2025)).

Though this is correlated with colour, it propagates in (different) complex ways for stars and galaxies (See Meyers & Burchat 2015). We approximate this effect. Considering only the colour difference between stars in the PSF model and galaxies (and not SEDs), we investigate the impact of this ”mean-colour DCR error” on cosmic shear. The errors due to this mean-colour DCR error are additive and can typically be represented as,

$$\gamma_{\mathrm{obs}} = \gamma_{\mathrm{true}} + \beta \delta \mathbf{e}^{\mathrm{DCR}}$$

to second order, where $\beta$ is calculated from the rho-statistics and tau-statistics and quantifies the impact from PSF modeling error on shape modeling errors (E.g. Gatti et al., 2021)]. Typically, $\beta$ is of order 1. Therefore, ignoring chance correlations $\langle \gamma_{\mathrm{true}} \delta \mathbf{e}^{\mathrm{DCR}} \rangle$, and choosing $\beta = 1$, the impact on the cosmic shear is approximately,

$$\langle \gamma_{\mathrm{obs}} \gamma_{\mathrm{obs}} \rangle \approx \langle \gamma_{\mathrm{true}} \gamma_{\mathrm{true}} \rangle + \langle \delta \mathbf{e}^{\mathrm{DCR}} \delta \mathbf{e}^{\mathrm{DCR}} \rangle.$$

In practice, we can forecast this impact as follows. As shown in Figure 5 & 6, the $\delta \mathbf{e}^{\mathrm{DCR}}$ due to DCR is determined empirically using a test set PSF star exposures reserved from the modeling.

The values $\mathrm{DCR}_1$ and $\mathrm{DCR}_2$ themselves can also be determined from the time, RA and Dec of observation and through Equation 1. From the LSST survey scheduler OpSim Baseline v5.1.0, we find this information for each exposure, calculate and tile the DCR values across the exposure field of view (approximated as a circle of radius 1.75°), and finally aggregate them into a HEALPix map of the sky weighted by the effective exposure time $T_{\mathrm{eff}} \times$ visitExposureTime. This is shown in Figure 11.

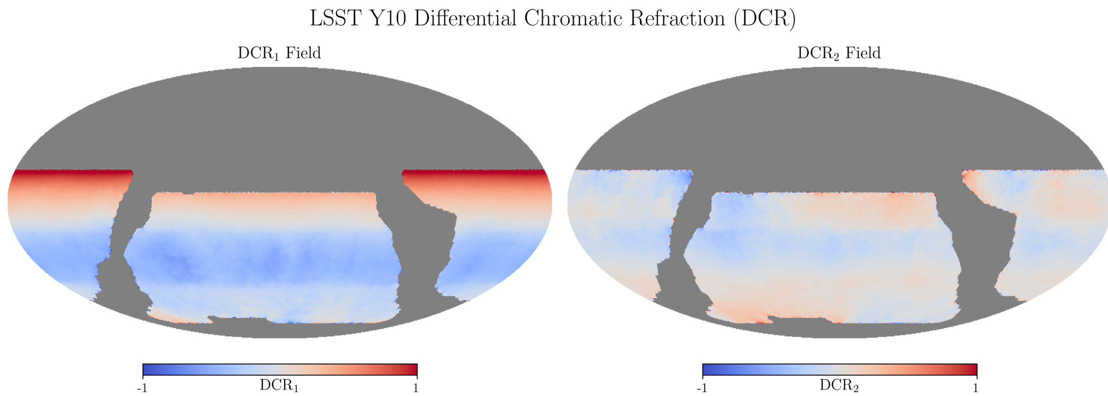


Figure 11: Differential Chromatic Refraction maps for LSST Y10 WFD using OpSim Baseline v5.1.0.

The mean-colour DCR error is a function of the colour difference between the average PSF star and galaxies. Therefore, higher redshift galaxies that are redder have greater DCR effect. We estimate the average range of source galaxy colours in LSST redshift bins using galaxies from DES. To do so, we draw galaxies from the DES into LSST redshift bins and use their colour distribution for LSST. Given that LSST goes to higher redshifts than DES, this works for all but the last redshift bin. For this bin, we linearly extrapolate the galaxy colours out to high redshift. This assumption is likely the largest source of inaccuracy in the forecasts for this redshift bin (bin 5), as the slope of the $\mathrm{DCR} - \delta e$ relation itself is sensitive to the $r - z$ colour of the galaxies. Additionally, as the Balmer break shifts out of the $z$ band at $z \approx 1.5$, it is unlikely that the galaxy colours increase linearly. However, for a worst-case forecast, this is a reasonable assumption.

Finally, we linearly fit the colour-dependent DCR–$\delta e$ relation for the uncorrected and corrected chromatic PSF case, and apply it to the DCR maps (Figure 11). To calculate the two-point correlation function of this error map, we use the `treecorr` software (Jarvis et al., 2004). We create a catalog from pixels, and perform the correlation $\langle \delta \mathbf{e}^{\mathrm{DCR}} \delta \mathbf{e}^{\mathrm{DCR}} \rangle$ for a range from 2.5 to 1000 arcmin, with 26 bins (to mimic DES within its range), and a `bin_slop` of 0.1. To forecast the shear signal and uncertainty, we use `GLASS` (Tessore et al., 2023), alongside the redshift distributions forecast by the LSST Science Requirements Document (The LSST Dark Energy

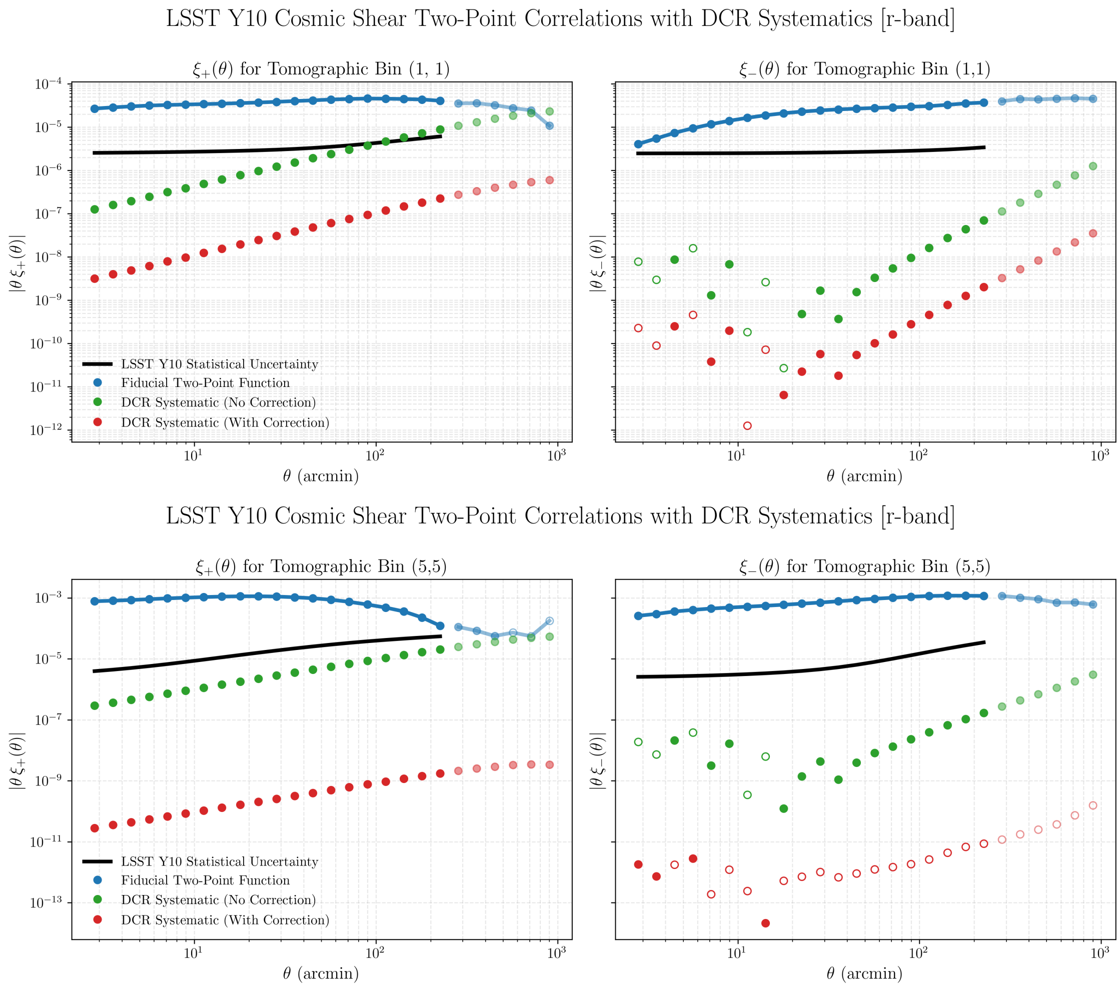


Figure 12: Impact of mean-colour DCR error on the cosmic shear two-point correlation function, for *r* band PSF exposures. In blue, we show the fiducial cosmic shear for the closest and furthest tomographic bin autocorrelation (1, 1) and bin (5, 5). The black line represents the uncertainty of cosmic shear from analytic covariance, for comparison. Data points beyond the DES cosmology range are faded. The DCR Systematic $\langle \delta \mathbf{e}^{\mathrm{DCR}} \delta \mathbf{e}^{\mathrm{DCR}} \rangle$ if uncorrected (shown in green) is below LSST Y10 statistical uncertainty for $\xi_+$ and $\xi_-$. The corrected DCR signal shown in red sufficiently reduces this effect by four orders of magnitude.

Science Collaboration et al., 2018) and `CosmoCov` (Krause & Eifler, 2017; Fang et al., 2020) to estimate the analytic uncertainty. These results are shown in Figure 12 for *r* band exposures and Figure 13 for *g* band exposures.

We find that the mean-colour DCR systematic indeed has a non-negligible impact on $\xi_+$ when considering the better *r* band exposures, where for Y10 of the LSST survey, systematic uncertainties would have been on the level of statistical uncertainties for the (1, 1) tomographic bin

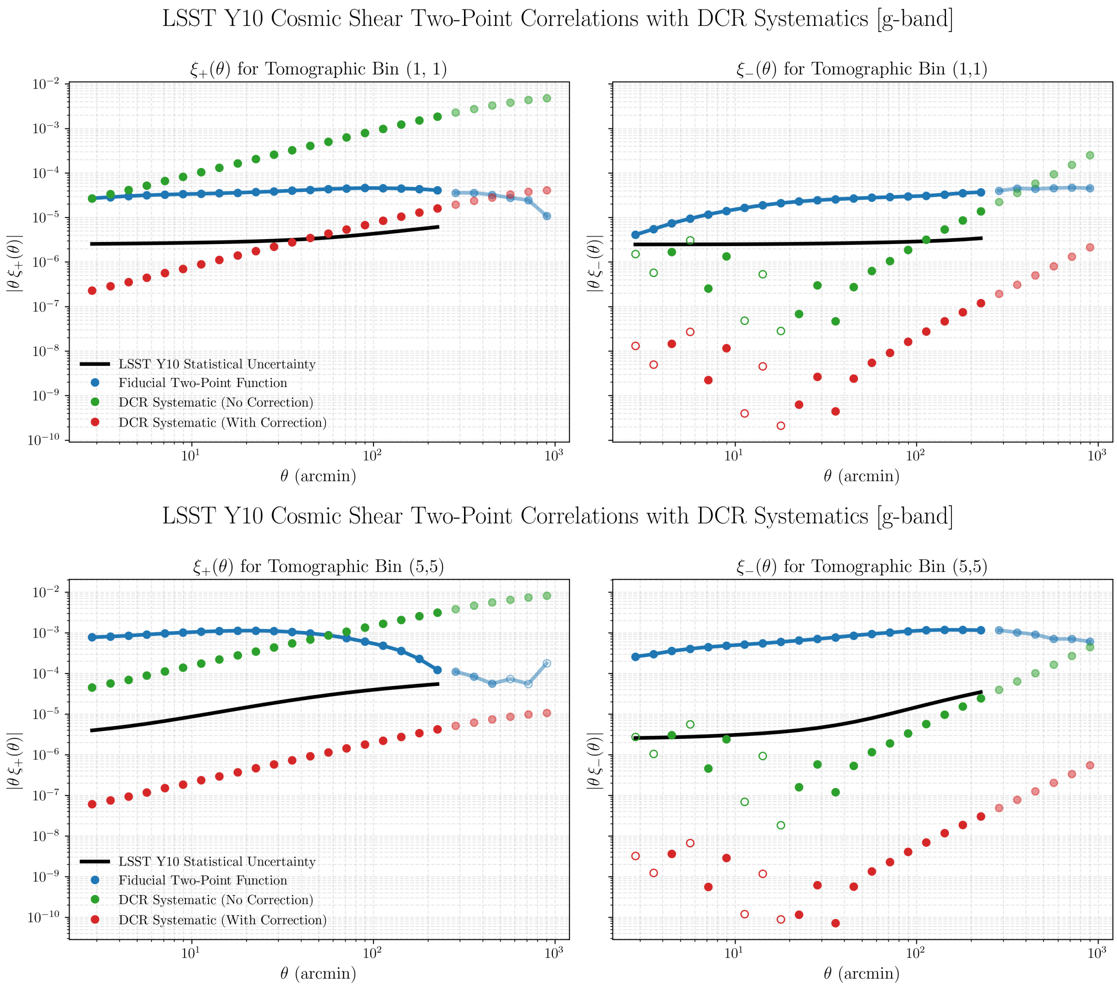


Figure 13: Impact of mean-colour DCR error on the cosmic shear two-point correlation function, for the poorer $g$ band PSF exposures. See Figure 12 for format. The DCR Systematic $\langle\delta\mathbf{e}^{\mathrm{DCR}}\delta\mathbf{e}^{\mathrm{DCR}}\rangle$ if uncorrected (shown in green) will dominate the cosmic shear signal for $\xi_+$ and even bias $\xi_-$ if only uncorrected $g$ band exposures are used. The corrected DCR signal shown in red reduces this effect, but may still impact bin (1, 1) at scales $\theta > 50$ arcmin.

correlation on large scales $\theta > 50$ arcmin. Correcting for the chromatic PSF using PiFF colour-dependence sufficiently reduces this systematic by four orders of magnitude. Post-correction, on all scales, mean-colour DCR effects in $r$ band remain subdominant to statistical errors.

The mean-colour DCR systematic on $g$ band exposures, however, is significant. Uncorrected, for $\xi_+$ the error is on the order of the cosmic shear signal itself. For $\xi_-$, the error is on the order of statistical uncertainties for small and large scales. Post-correction, though the systematic is reduced by two to three orders of magnitude, the systematic error remains high for the (1,

1) autocorrelation on scales $\theta \gtrsim 50$. This can be directly attributed to the order of magnitude higher DCR error in *g* band in the DCR $-\delta e$ relation (Compare figures 5 & 6). Given this, it is not recommended to use *g* band, similar to DES (Jarvis et al., 2021; Schutt et al., 2025), for which the *g* band error is similarly an order of magnitude above *r* band errors (Figure 10).

Further detailed study of the forecasted impact of DCR and other shape systematics for LSST will be presented in Agarwal et al. (in prep).

## 8 Conclusions

In this note, we have evaluated the impact of enabling chromatic PSF modeling during commissioning of the Vera C. Rubin Observatory using weekly-processed DRP data (`w_2025_49`). By incorporating colour-dependent terms into the `PiFF` PSF model, we directly address wavelength-dependent effects, in particular Differential Chromatic Refraction (DCR), which is expected to be one of the dominant chromatic systematics in ground-based weak lensing measurements.

Using ∼153 million stellar measurements across 4898 visits, we have shown that enabling a second-order polynomial dependence in both spatial position and colour substantially improves PSF residuals:

- **Residuals vs. magnitude:** Chromatic fitting significantly reduces the spread in PSF size and ellipticity residuals between colour bins, particularly in the faint regime. In the *g* band, where DCR is strongest, residuals in $\delta T/T$ decrease by ∼50%, and faint-end ellipticity residuals tighten by up to ∼75%.
- **Residuals vs. colour:** The strong colour dependence observed in the non-chromatic configuration is largely mitigated in the *g* band when chromatic fitting is enabled. Remaining trends in the *u* band are likely driven by limited stellar statistics in the reddest colour bins rather than fundamental modeling limitations.
- **Residuals vs. DCR:** The most dramatic improvement is seen in DCR-dependent trends. In the *g* band, chromatic PSF modeling reduces DCR-correlated ellipticity residuals by up to ∼90–95%, effectively suppressing these systematics by nearly an order of magnitude. Improvements in the *r* band are more modest (∼50%) but still significant.

When compared to Dark Energy Survey (DES) Year 6 results, Rubin commissioning data with chromatic PSF fitting achieves residual levels that are comparable to, and in some cases improved relative to, DES. In particular, DCR-dependent ellipticity residuals in the $g$ band are suppressed to levels that outperform DES by up to ∼80%, demonstrating that the Rubin PSF modeling framework is already competitive at the commissioning stage.

Finally, we propagated DCR-induced PSF residuals to forecasts of cosmic shear systematics. Without chromatic correction, the induced additive systematic $\langle \delta e_{\mathrm{DCR}}\, \delta e_{\mathrm{DCR}} \rangle$ can be comparable to or exceed the expected LSST Year 10 statistical uncertainty in the most affected tomographic bins. With chromatic PSF modeling enabled, this contribution is reduced by approximately two orders of magnitude, bringing the DCR-induced shear systematic well below the statistical error budget across relevant angular scales.

## A Acknowledgements

This material is based upon work supported in part by the National Science Foundation through Cooperative Agreements AST-1258333 and AST-2241526 and Cooperative Support Agreements AST-1202910 and AST-2211468 managed by the Association of Universities for Research in Astronomy (AURA), and the Department of Energy under Contract No. DE-AC02-76SF00515 with the SLAC National Accelerator Laboratory managed by Stanford University. Additional Rubin Observatory funding comes from private donations, grants to universities, and in-kind support from LSST-DA Institutional Members.

## B References

Agarwal, S., Chang, C., Giannini, G., Anbajagane, D., Drlica-Wagner, A., in prep, Impact of spatially varying systematic effects on shape measurements and cosmology: a study for des, decade and lsst,
In preparation

Burke, D.L., Rykoff, E.S., Allam, S., et al., 2018, AJ, 155, 41 (arXiv:1706.01542), doi:10.3847/1538-3881/aa9f22, ADS Link

Fang, X., Krause, E., Eifler, T., MacCrann, N., 2020, JCAP, 2020, 010 (arXiv:1911.11947), doi:10.1088/1475-7516/2020/05/010, ADS Link

Gatti, M., Sheldon, E., Amon, A., et al., 2021, MNRAS, 504, 4312 (arXiv:2011.03408), doi:10.1093/mnras/stab918, ADS Link

Hirata, C., Seljak, U., 2003, MNRAS, 343, 459 (arXiv:astro-ph/0301054), doi:10.1046/j.1365-8711.2003.06683.x, ADS Link

Jarvis, M., Bernstein, G., Jain, B., 2004, Monthly Notices of the Royal Astronomical Society, 352, 338, doi:10.1111/j.1365-2966.2004.07926.x

Jarvis, M., Bernstein, G.M., Amon, A., et al., 2021, MNRAS, 501, 1282 (arXiv:2011.03409), doi:10.1093/mnras/staa3679, ADS Link

Krause, E., Eifler, T., 2017, Monthly Notices of the Royal Astronomical Society, 470, 2100–2112, arXiv:1601.05779 [astro-ph], doi:10.1093/mnras/stx1261

Mandelbaum, R., Hirata, C.M., Seljak, U., et al., 2005, MNRAS, 361, 1287 (arXiv:astro-ph/0501201), doi:10.1111/j.1365-2966.2005.09282.x, ADS Link

Mandelbaum, R., Lanusse, F., Leauthaud, A., et al., 2018, MNRAS, 481, 3170 (arXiv:1710.00885), doi:10.1093/mnras/sty2420, ADS Link

Meyers, J.E., Burchat, P.R., 2015, ApJ, 807, 182 (arXiv:1409.6273), doi:10.1088/0004-637X/807/2/182, ADS Link

Meyers, J.E., Burchat, P.R., 2015, ApJ, 807, 182 (arXiv:1409.6273), doi:10.1088/0004-637X/807/2/182, ADS Link

Plazas, A.A., Bernstein, G., 2012, PASP, 124, 1113 (arXiv:1204.1346), doi:10.1086/668294, ADS Link

**[PSTN-019]**, Rubin Observatory Science Pipelines Developers, 2025, *The LSST Science Pipelines Software: Optical Survey Pipeline Reduction and Analysis Environment*, Project Science Technical Note PSTN-019, NSF-DOE Vera C. Rubin Observatory, URL https://pstn-019.lsst.io/, doi:10.71929/rubin/2570545

Schutt, T., Jarvis, M., Roodman, A., et al., 2025, The Open Journal of Astrophysics, 8, 26 (arXiv:2501.05781), doi:10.33232/001c.132299, ADS Link

**[DMTN-017]**, Sullivan, I.S., Reiss, D.J., 2015, *Differential Chromatic Refraction: literature overview*, Data Management Technical Note DMTN-017, NSF-DOE Vera C. Rubin Observatory, URL https://dmtn-017.lsst.io/

Tessore, N., Loureiro, A., Joachimi, B., von Wietersheim-Kramsta, M., Jeffrey, N., 2023, The Open Journal of Astrophysics, 6, 11 (arXiv:2302.01942), doi:10.21105/astro.2302.01942, ADS Link

The LSST Dark Energy Science Collaboration, Mandelbaum, R., Eifler, T., et al., 2018, arXiv e-prints, arXiv:1809.01669 (arXiv:1809.01669), doi:10.48550/arXiv.1809.01669, ADS Link

## C Acronyms

| Acronym | Description |
|---|---|
| AST | NSF Division of Astronomical Sciences |
| AURA | Association of Universities for Research in Astronomy |
| B | Byte (8 bit) |
| CCD | Charge-Coupled Device |
| COSMOS | Cosmic Evolution Survey |
| DCR | Differential Chromatic Refraction |
| DE-AC02 | Department of Energy contract number prefix |
| DECam | Dark Energy Camera |
| DES | Dark Energy Survey |
| DM | Data Management |
| DMTN | DM Technical Note |
| DRP | Data Release Processing |
| ECDFS | Extended Chandra Deep Field-South Survey |
| EDFS | Euclid Deep Field South |
| FGCM | Forward Global Calibration Method |
| HEALPix | Hierarchical Equal-Area iso-Latitude Pixelisation |
| HSM | Hierarchical Storage Management |
| LSST | Legacy Survey of Space and Time |
| LSST-DA | LSST Discovery Alliance |
| LSSTCam | LSST Science Camera |
| OpSim | Operations Simulation |
| PSF | Point Spread Function |

| | |
|---|---|
| PSTN | Project Science Technical Note |
| RA | Rapid Analysis |
| RSP | Rubin Science Platform |
| SED | Spectral Energy Distribution |
| SI | System and Information Integrity |
| SLAC | SLAC National Accelerator Laboratory |
| US | United States |
| USDF | United States Data Facility |
| WFD | Wide-Fast-Deep |

# D Alternate PSF Fitting Configurations

## D.1 Spatial Order 2, Colour Order 1

This section shows plots with the following fitting configuration. We use the same spatial order as Sec. 5 but reduce the colour order from 2 to 1.

```
config.psf_determiner['piff'].spatialOrderPerBand = {
  "u": 2, "g": 2, "r": 2, "i": 2, "z": 2, "y": 2,
}
config.psf_determiner['piff'].zerothOrderInterpNotEnoughStars = False
config.psf_determiner['piff'].piffBasisPolynomialSolver = "cpp"
config.psf_determiner['piff'].piffPixelGridFitCenter = False
config.psf_determiner['piff'].useColor = True
config.psf_determiner['piff'].colorOrder = 1
config.psf_determiner['piff'].color = {
  "u": "g-i", "g": "g-i", "r": "g-i", "i": "g-i",
  "z": "i-z", "y": "i-z",
}
```

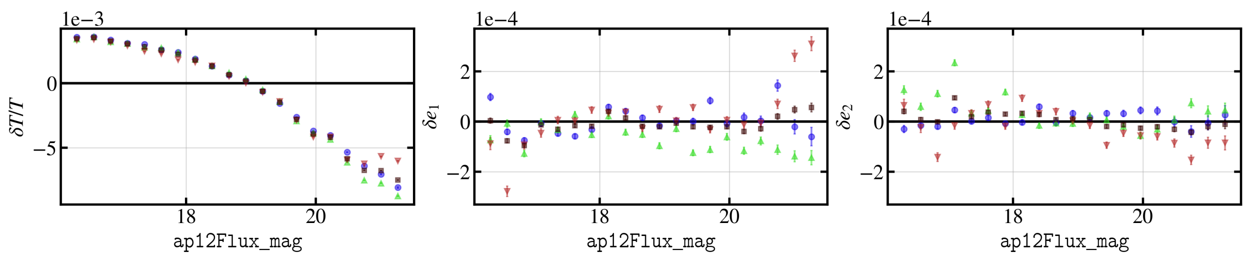


(a) PSF residuals across all bands vs. magnitude, with chromatic fitting.

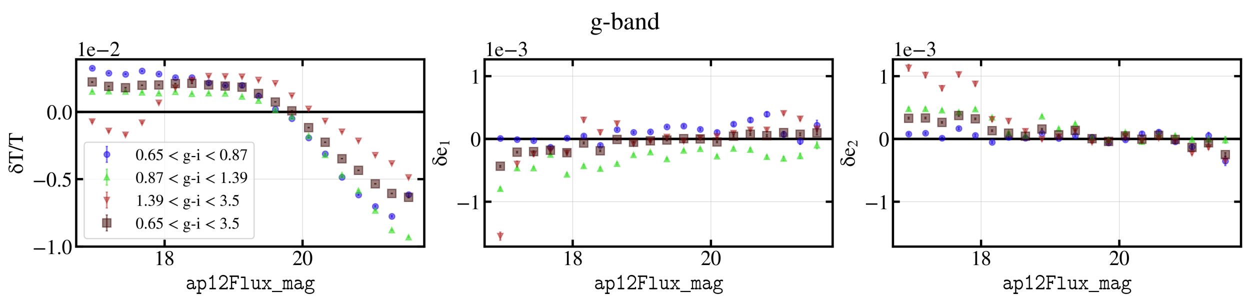


(b) $g$ band PSF residuals vs. magnitude, with chromatic fitting.

Figure 14: Residuals as a function of ap12Flux_mag after chromatic fitting with colour order 1. Stars are divided into equal-sized colour bins of $g - i \in [0.65, 0.87, 1.39, 3.5]$. There are no significant differences between this configuration and the configuration used in Subfigs. 2b and 3b.

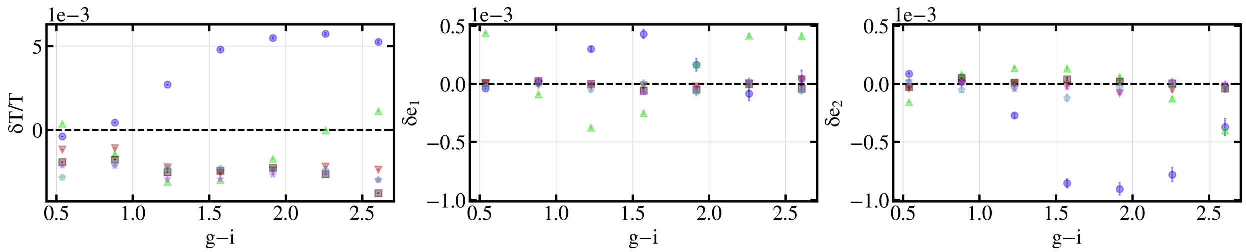


(a) with chromatic PSF fitting.

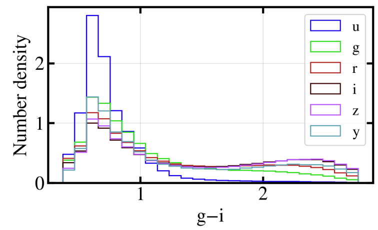


(b) Number density as a function of $g-i$ colour.

Figure 15: PSF residuals as a function of $g-i$ colour. The $u$ and $g$ band residuals show the highest dependence on $g-i$ colour. The $g$ band residual is not corrected as well here as it is with colour order 2 in Subfig. 4b.

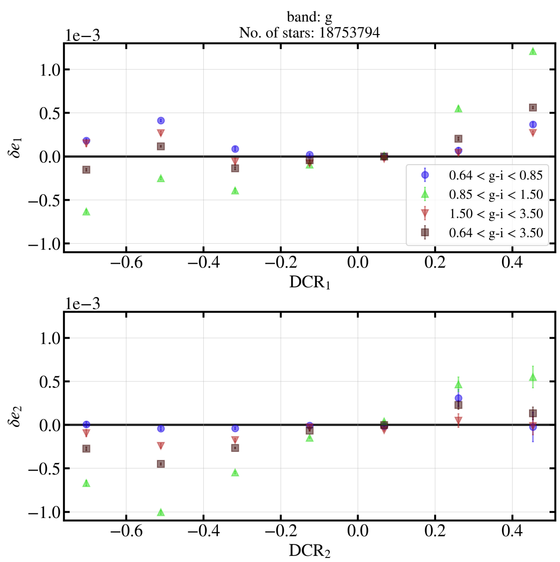


(a) DCR in the $g$ band after chromatic fitting.

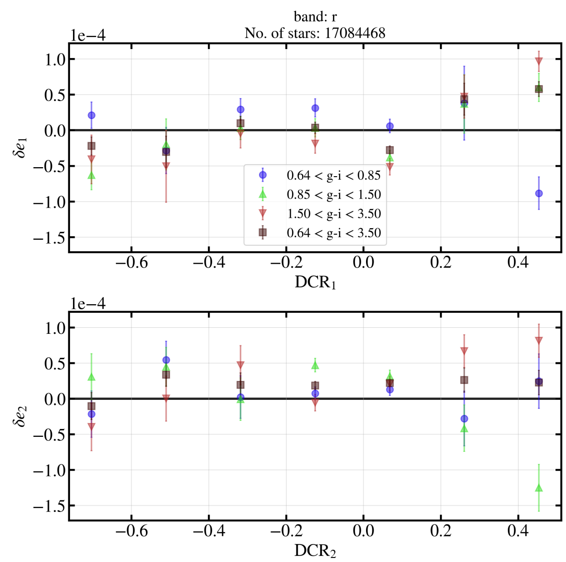


(b) DCR in the $r$ band after chromatic fitting.

Figure 16: PSF $\delta e_1$ and $\delta e_2$ as a function of $\mathrm{DCR}_1$ and $\mathrm{DCR}_2$. Residuals in the $g$ band are ∼50% larger than when using colour order 2 in Subfig. 5b. Residuals in the $r$ band are on a comparable level to those in Subfig. 6b.

# E Parallactic Angles

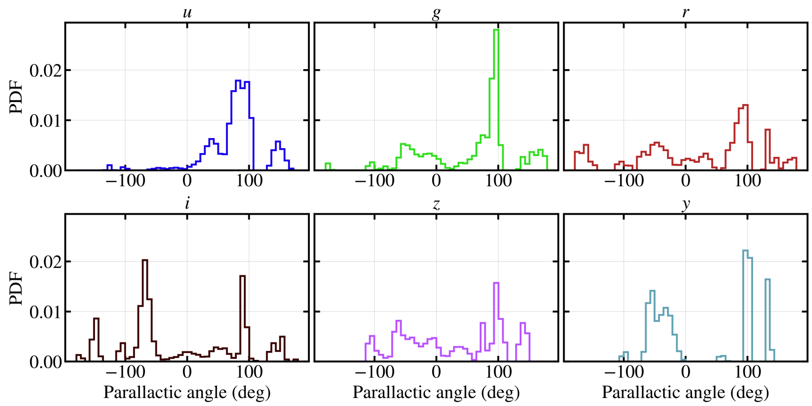


(a)

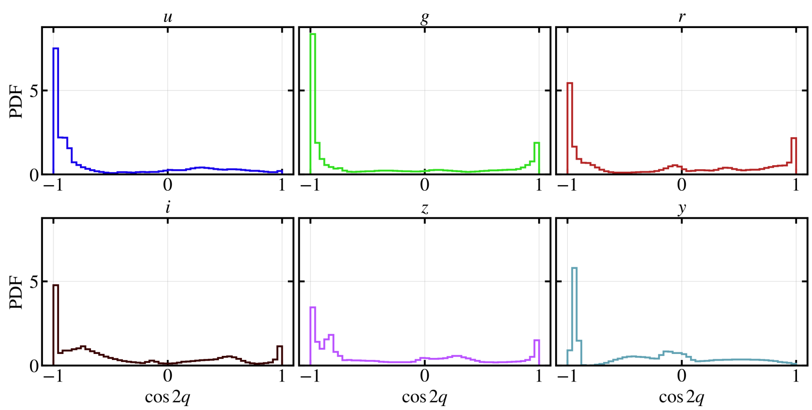


(b)

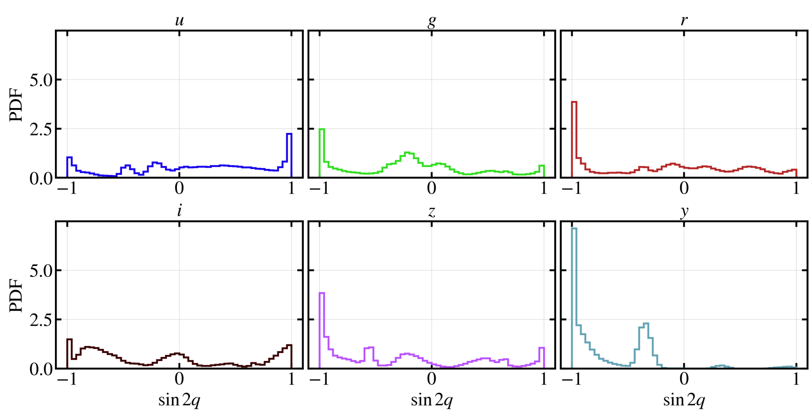


(c)

Figure 17: Subfigure 17a plots the distribution of parallactic angles in the week 49 DRP, and Subfigs. 17b and 17c plot $\cos 2q$ and $\sin 2q$ respectively.